Nano Energy 63 (2019) 103840

Contents lists available at ScienceDirect

Nano Energy

journal homepage: www.elsevier.com/locate/nanoen

Full paper

Atomic-level tunnel engineering of todorokite MnO_2 for precise evaluation of lithium storage mechanisms by *in situ* transmission electron microscopy

Ran Cai[a,b,1], Shiying Guo[c,1], Qingping Meng[d,1], Shize Yang[e], Huolin L. Xin[e,f], Xiaobing Hu[g,h], Mingqiang Li[b], Yuanwei Sun[b], Peng Gao[b,**], Shengli Zhang[c,***], Hui Dong[a], Shuangying Lei[a], Kisslinger Kim[e], Haibo Zeng[c], Litao Sun[a,*], Feng Xu[a,****], Yimei Zhu[d]

[a] SEU-FEI Nano-Pico Center, Key Laboratory of MEMS of Ministry of Education, Southeast University, Nanjing, 210096, China
[b] Electron Microscopy Laboratory, and International Centre for Quantum Materials, School of Physics, Peking University, Beijing, 100871, China
[c] College of Materials Science and Engineering, Nanjing University of Science and Technology, Nanjing, 210094, China
[d] Energy Sciences Directorate, Brookhaven National Laboratory, Upton, NY, 11973, USA
[e] Center for Functional Nanomaterials, Brookhaven National Laboratory, Upton, NY, 11973, USA
[f] Department of Physics and Astronomy, University of California, Irvine, CA, 92697, USA
[g] Department of Materials Science and Engineering, Northwestern University, Evanston, IL, 60208, USA
[h] NUANCE Center, Northwestern University, Evanston, IL, 60208, USA

ARTICLE INFO

Keywords:
Atomic-precise structure engineering
Todorokite MnO_2
Lithiation mechanism
In situ transmission electron microscopy
Reciprocating-motion reaction front

ABSTRACT

Todorokite-type manganese oxide (τ-MnO_2) with p × 3 tunneled structure is especially captivating as charge storage material for rechargeable batteries, since the enlarged tunnel dimensions enable rapid electrode kinetics and superior rate performance. However, its congenitally rich polytypism associated with tunnel heterogeneity impedes our precise understanding of structure-property relationship in this polytypic material. In this regard, this work has taken substantial effort to preliminarily achieve uniform 4 × 3 tunnel-structured τ-MnO_2 nanorods, as corroborated via atomically resolved imaging. Afterwards, the (de)lithiation mechanisms of the tunnel-specific phase are investigated via *in situ* transmission electron microscopy including electron diffraction, high-resolution imaging, and electron energy loss spectroscopy, coupled with density functional theory calculations and phase field simulations. Upon initial lithiation, the intercalation reaction region β (less than 1.43 Li insertion) is observed as result of rapid lithium-ion diffusion through the tunnels with slightly increased lattice constants. By tracing the full lithiation procedure, the evolution of intermediate Mn_2O_3 phase and the development of final Mn and Li_2O phases are identified in the conversion reaction region α (more than 1.43 Li insertion). These results indicate that τ-MnO_2 can be applied to a cathode by intercalation reaction and to an anode by conversion reaction in corresponding to voltage ranges in a lithium-based battery. Upon delithiation, we observe an unusual reciprocating-motion reaction front (different from one-way lithiation reaction front), for which the driven dynamics are delineated based on a phase field model. Impressively, a reversible and symmetric conversion reaction between Mn_2O_3 phase and Mn + Li_2O phases is established upon subsequent (de)lithiation cycles. This work can be regarded as a stepping-stone arousing the appetite of a comprehensive understanding of the highly polytypic material with other tunnel-specific phases.

1. Introduction

Tunnel-structured manganese dioxides (MnO_2) have attracted considerable attention because of their potential applications in heterogeneous catalysis, chemical absorption, molecular sieving, and ion-exchange [1–4]. Typically, the open tunnel frameworks of these materials are composed of edge- and corner-sharing MnO_6 octahedra, with internal tunnels being occupied by cations and water molecules

* Corresponding author.
** Corresponding author.
*** Corresponding author.
**** Corresponding author.
E-mail addresses: p-gao@pku.edu.cn (P. Gao), zhangslvip@njust.edu.cn (S. Zhang), slt@seu.edu.cn (L. Sun), fxu@seu.edu.cn (F. Xu).
[1] These authors contributed equally to this work.

https://doi.org/10.1016/j.nanoen.2019.06.036
Received 8 May 2019; Received in revised form 15 June 2019; Accepted 15 June 2019
Available online 24 June 2019

[5]. Such manganese dioxides, e.g., todorokite MnO_2 (τ-MnO_2) [6] and hollandite MnO_2 (α-MnO_2) [7], are fascinating as charge storage materials for rechargeable batteries with high-rate capability, because the unique 1D tunnels enable fast reversible insertion/extraction of charge carriers [8–10].

As a promising electrode candidate used in lithium-ion batteries (LIBs), the lithiation mechanism of the α-MnO_2 has been investigated in depth, while little is known about the τ-MnO_2 so far. Compared with the α-MnO_2 with 2 × 2 tunnels (this naming law is based on the numbers of the MnO_6 octahedra constructing the tunnel height and width, respectively) [11–13], the intrinsically polytypic τ-MnO_2 has larger tunnels with p × 3 dimensions (p ≥ 3) [14–16], which likely enables easier and faster ionic transport and electrode reaction kinetics within the τ-MnO_2 material. Additionally, the tunnels in τ-MnO_2 are well ordered continuously along the *b* direction [17], rather than along the *c* axis in the case of α-MnO_2 [18]. These structural differences could possibly result in disparate lithiation behaviors and lithium storage mechanisms. Early works have revealed a maximum storage of 0.6 Li per Mn in τ-MnO_2 and focused on the low lithiation levels for the cathode application [16,19].

Very recently, several research groups have revisited the τ-MnO_2 via advanced atomically resolved imaging, attempting to unveil the underlying structural origin behind the rich polytypism of this material. Hu et al. have demonstrated that Mg^{2+}-stabilized τ-MnO_2 should not be simplistically seen as a pure 3 × 3 tunnel structure but rather as a polytypic p × 3 family, where p is an integer generally less than or equal to 6, with 3 × 3, 4 × 3, and 5 × 3 tunnels appearing most frequently [15]. Soon afterwards, Yuan et al. have pointed out that the tunnel heterogeneity within single τ-MnO_2 nanorods possibly affects the energy storage kinetics even down to sub-nanometer scale [20]. Further, they have corroborated such an effect in the case of single α-MnO_2 (instead of the τ-MnO_2) nanorods with the coexistence of 2 × 2 and 2 × 3 tunnels. Additionally, the theory calculations from Li et al. have indicated that the origin of tunnel heterogeneity of τ-MnO_2 could be traced back to the layer-to-tunnel transition stage, thus calling for renewed attention to preparation of high-quality precursors [21]. Despite these efforts, a precise (de)lithiation mechanism associated with tunnel-specific phases of the τ-MnO_2 still remains largely unknown as the highly polytypic nature of this material impedes the thorough understanding of a precise structure-property relationship, which motivates our present work.

In this report, we first demonstrated the as-synthesized Mg^{2+}-doped τ-MnO_2 nanorods (NRs) featuring a high percentage of 4 × 3 tunnels (9.2 × 6.9 Å dimensions), as identified via spherical aberration-corrected scanning transmission electron microscopy (Cs-STEM). Afterwards, the entire lithiation-delithiation cycles of τ-MnO_2 NRs were observed 'operando' by using *in situ* transmission electron microscopy. Real-time high-resolution observations were utilized to track the movement of reaction fronts, and electron diffraction (ED) and electron energy-loss spectroscopy (EELS) were employed to identify the microstructure and valence of the reacting phases. Upon initial lithiation, we observed the one-way motion of two distinct lithiation reaction fronts (RFs) that highlighted intercalation reaction and conversion reaction interfaces, respectively. Lithium intercalation was initiated with formation of intermediate phase Mn_2O_3 that is subsequently converted to metallic Mn and Li_2O phases characterized by substantial volume expansion. We also notice a limited lateral ($a-c$ oriented) transfer of Li^+ between NRs, which is slightly different from the previous finding in the case of 2 × 2 tunneled α-MnO_2. These experimental findings are also supported from density functional theory (DFT) calculations. Furthermore, we discovered an unusual reciprocating-motion RF upon delithiation, for which the driven dynamics were revealed by employing a phase field model. To the best of our knowledge, this is the first time-resolved visualization of the reciprocating-motion delithiation RF, suggesting that the delithiated product could undergo a prenucleation stage directly associated with different degrees of lithium removal. Subsequently, a symmetric and reversible phase transformation between Mn_2O_3 and Mn phases would be established upon repeated cycles. The present work aims at the precise evaluation of energy storage mechanism in certain tunnel-specific phase of the polytypic τ-MnO_2 and may provide a paradigm shift for a comprehensive understanding of the structure-property relation in other tunnel-structured τ-MnO_2 materials.

2. Experimental section

2.1. Material synthesis and characterization

The tunnel-structured τ-MnO_2 NRs were formed by autoclaving high-quality layer-structure manganese oxides [22,23], which were first prepared using a method modified by us. The nature and thermal stability of tunnel structured products depend strongly on high-quality precursors, which were decided by preparation parameters, such as the temperature, pH, and aging time. Briefly, 50 mL of 1 M H_2O_2 and 50 mL of 0.5 M NaOH were mixed and then added to 50 mL of 0.3 M $Mn(NO_3)_2$ under stirring for 1 h under ice-water bath. After that, the precipitate of Na-birnessite manganese oxide was obtained by filtration and washing with deionized water. Subsequently, the obtained Na-birnessite precipitate was dispersed in 1 L of 1 M $MgCl_2$ solution for 48 h to replace Na^+ ions with Mg^{2+} ions. Afterwards, the precipitate was filtered, washed with H_2O, and dispersed in another 1 L of 1 M $MgCl_2$ solution. The ion exchange process was repeated three times for a thorough phase transformation from Na-birnessite to Mg-buserite. After filtration and washing, 50 mg of Mg-buserite in was dispersed in 17 mL of 1 M $MgCl_2$ solution and then the mixture was transferred into a Teflon-lined stainless steel autoclave for a 96 h of hydrothermal reaction at 220 °C. Finally, the τ-MnO_2 NRs were obtained by filtration, washing, and drying at 100 °C for 12 h. Phase identification and surface morphology of τ-MnO_2 were characterized by a powder X-ray diffractometer (ARLXTRA, Thermo Electron Co., USA) and a scanning electron microscope (JSM-7600F, JEOL, Japan, Fig. S1 (Supplementary material). Cross–section specimens of τ-MnO_2 NRs were prepared using a commercially available FIB system (SIM9200: Seiko Instrument Inc.) with a beam of 30 keV Ga^+ ions.

2.2. Electron microscopy characterization

Atomic resolution high angle annular dark field (HAADF) imaging from the lateral direction, electron diffraction, EEL spectroscopy and EDS line scanning were performed using a double aberration-corrected FEI Titan Them G2 microscope operated at 300 kV. The beam current is ~40 pA. The convergence semi-angle is 21 mrad. And the collection semi-angle snap in the range of 80–379 mrad. EEL spectrum data were recorded in scanning TEM (STEM) mode with a convergence angle of 21 mrad and a collection angle of 90 mrad. The energy resolution of EEL spectrum measurement was around 0.25 eV. Atomic resolution high angle annular dark field (HAADF) imaging from axial direction was carried out using FEI Talos F200X with an X-FEG electron source module and operated at 200 keV in Brookhaven National Laboratory. The high source brightness enables near diffraction limited imaging and dramatically improves the spectroscopic performance.

2.3. In situ TEM (de)lithiation

A high-resolution microscope (FEI Tecnai F20, 200 kV) with an One View IS (Gatan) camera with frame rates up to 400 frames per second was carried out for *in situ* observing the electrochemical behaviors of the τ-MnO_2 NRs during lithiation/delithiation cycles with the assistance of electron diffraction patterns and HRTEM images. The details of electrochemical experiment setup inside TEM are described as following. The τ-MnO_2 NRs were attached to a half copper grid by conductive silver colloid to ensure a good electrical contact. Metal lithium

was regarded as the counter electrode and lithium source and adhered to a sharp grounded tungsten tip that was associated to a piezo-driven biasing-probe built into the STM-TEM sample holder (Nanofactory Instruments and PicoFemto). The natural oxide layer Li_2O which was generated in the holder loading process acted as the role of solid electrolyte [24], allowing the transport of lithium ions. All these processes were accomplished in a glovebox filled with Ar-gas, as lithium is a very active metal and can be oxidized easily. Afterward, the holder was immediately transferred into TEM column. A constant −1.5 V/1.5 V potential was then applied to the τ-MnO_2 NRs with respect to lithium counter electrode to drive the transport of lithium ions through the solid-state electrolyte Li_2O layer, thereby initiating the electrochemical lithiation/delithiation process. In situ electric biasing experiments were carried out using the Nanofactory piezo-controlled sample holder and Pico Femto holder in Peking University.

2.4. DFT calculations

All DFT calculations were performed by generalized gradient approximation (GGA) parameterized by the Perdew, Burke, and Ernzerhof (PBE) functional, as implemented in the Vienna Ab initio Simulation Package (VASP) [25–27]. The DFT + U corrections was applied to 3d orbitals of Mn [28–30]. Spin polarized was also included in all calculations. The energy cutoff for the plane-wave basis set was 450 eV and the Brillouin zone was sampled by 4 × 1 × 7. The electronic iterations convergence criterion was set as 10^{-4} eV in energy and 0.01 eVÅ^{-1} in force. The initial structure of τ-MnO_2 includes twenty-eight manganese atoms with two large 4 × 3 tunnels and two 1 × 1 tunnels. And it also includes eight magnesium atoms and sixteen water molecules within the tunnels. The optimized parameters of τ-MnO_2 are a = 23.20 Å, b = 5.36 Å, and c = 9.14 Å, respectively, which are consistent with the observed the interplanar spacings in Fig. 1.

2.5. Electrochemical characterization

The electrochemical performance of as-prepared materials was investigated by coin cells. Binder free self-supporting (BFSS) electrodes of τ-MnO_2 NRs, metallic lithium foils, and electrolyte consisting of 1 M $LiPF_6$ in ethylene carbonate-dimethylcarbonate (1:1 in volume) were employed in the cells. Galvanostatic discharge-charge profile was acquired with a current density of 0.1 A g^{-1} in the voltage range of 0.01–4 V using a multichannel battery test system (LAND CT2001A). Cyclic voltammetry (CV) test was conducted in the voltage range of 0.01–3.0 V with a scan rate of 0.1 mV s^{-1}.

2.6. Phase field calculations

The evolution of the microstructure of experimentally observed were modeled by the phase field theory based on nonequilibrium thermodynamics developed by Bazant and his collaborator [31]. In that framework, at the surface of a crystal, the standard phenomenological model of electrode kinetics can be expressed by the Butler-Volmer equation [31,32]:

$$\frac{\partial c}{\partial t} = \frac{I_0}{ne}\left[\exp\left(-\frac{\alpha ne\eta}{k_B T}\right) - \exp\left(\frac{(1-\alpha)ne\eta}{k_B T}\right)\right] \quad (1)$$

where $\frac{\partial c}{\partial t}$ is the change rate of the local filling fraction c of Li-ion; α, the electron-transfer symmetry factor, is approximately constant for many reaction; η is activation overpotential; ne is the net charge transferred from the solution to the electrode; k_B is the Boltzmann's constant and T is the temperature; I_0 is the exchange current which can describe the inserted or extracted rate of Li-ion. Based on the Cahn-Hilliard phase field model [32],

$$\frac{\delta G}{\delta c} = \frac{\partial f}{\partial c} - \kappa\nabla^2 c \quad (2)$$

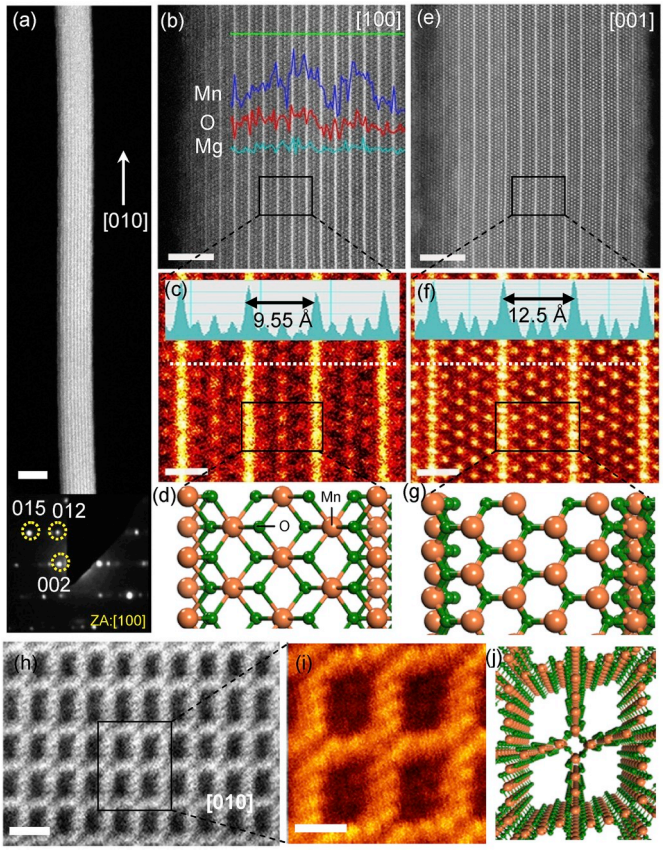

Fig. 1. Basic structure characterization of τ-MnO_2 NRs. (a) A low-magnification HAADF-STEM image of a single τ-MnO_2 NR with a diameter of 35 nm along [010] direction. Inset shows the corresponding electron ED pattern viewed along [100] zone axis. Scale bar, 30 nm. (b) The magnified HAADF-STEM image of the same τ-MnO_2 NR. The green line, along which EDS line scanning was carried out, indicates the region consists of three elements of Mn, O and Mg. Scale bar, 2 nm. (c) Atomic resolution HADDF-STEM image and (d) the corresponding atomic structure model of the area in b (dark rectangle). The brightest lattice planes correspond to rows and columns of Mn (MnO_6) atoms which constitute the tunnel framework. Intensity profile (inset of c) along the white dashed line shows the interplanar spacing of brightest lattice plane is 9.55 Å. Three other lattice planes are clearly observed between the bright planes, indicating three MnO_6 octahedra on the c side per unit cell. Scale bar, 1 nm. (e) The magnified HAADF-STEM image of τ-MnO_2 NR viewed along [001] zone axis. Scale bar, 2 nm. (f) Atomic resolution HADDF-STEM image and (g) atomic structure model of the area in e (dark rectangle). Scale bar, 1 nm. Four other lattice planes between the bright planes and the intensity profile (inset of f) along the white dashed line confirms four MnO_6 octahedra on a side with a dimension of 12.5 Å. (h) Cross-sectional HAADF-STEM image of τ-MnO_2 NR viewed along the [010] axis. Scale bar, 2 nm. (i) Atomic resolution HADDF-STEM image and (j) atomic structure model of the area in h (black rectangle). Scale bar, 1 nm. The orange ball indicates Mn atom, whereas the green presents O atom. The bright spots surrounding each tunnel refer to Mn (MnO_6) atomic columns, revealing 4 × 3 tunnels structure.

where f is the homogeneous free energy function; and κ is the Cahn-Hilliard gradient energy coefficient. The activation overpotential in Eq. (1) can be written as

$$\eta = \frac{\Delta\mu}{ne} \quad (3)$$

where $\Delta\mu$ is the thermodynamic driving force and is the self-consistent definition of diffusional chemical potential. For an inhomogeneous system, the simplest approximation is $\Delta\mu = \frac{\delta G}{\delta c}$.

Inside electrode, the Cahn-Hilliard equation determines the evolution of Li-ion concentration [33].

$$\frac{\partial c}{\partial t} = \nabla M c \nabla(\Delta\mu) \quad (4)$$

Where M is the Li mobility tensor, which is in general a function of Li concentration. We assign M to be a constant in our simulations. Details of the parameters chosen and the solutions to the model appear in the Supplementary material.

3. Results and discussion

The morphology and phase structure of as-synthesized τ-MnO_2 NRs were confirmed by SEM and XRD in Fig. S1 (Supplementary material). XRD pattern shows three diffraction peaks that can be indexed as (001), (002) and (004) planes of todorokite material belonging to the monoclinic space group $P2/m$ (JCPDS No.38–475) [34,35]. SEM images show that the NRs are high aspect ratio with diameters of 20–70 nm and lengths of several micrometers. Individual NRs tend to agglomerate along their longitudinal axes, forming thick bunches as a result of oriented attachment [24].

Further, the basic atomic structure of τ-MnO_2 NR from both the lateral and axial directions were identified using the Cs-STEM with a high-angle annular dark field (HAADF) detector. Fig. 1a shows a monocrystalline NR growing in the [010] direction with a uniform diameter. Fig. 1b shows a high-resolution HAADF-STEM image viewed along the NR [100] direction. The green line, along which EDS line scanning was carried out, indicates the region consists of three elements of Mn, O and Mg, and the chemical composition is found to be $Mg_{0.29}MnO_2{\cdot}0.5H_2O$. The brightest lattice planes in Fig. 1c correspond to Mn (MnO_6) atomic columns which constitute the tunnel framework. Three other lattice planes are clearly observed between the bright planes, indicating three MnO_6 octahedra on the c side per unit cell. In Fig. 1c, the intensity profile along white dashed line shows an interplanar spacing of 9.55 Å between the brightest lattice planes, agreeing well with the XRD result. Similarly, another HAADF-STEM image along the [001] direction confirms four MnO_6 octahedra on the a side with a dimension of 12.5 Å, as shown in Fig. 1e and f. Oxygen and hydrogen atoms are invisible in HAADF-STEM image due to the weak scattering power (lower Z) [18]. In Fig. 1d,g, both the atomic model structures (orange: Mn, green: O) along the NR [100] and [001] directions are well consistent with our atomic-resolution observations.

Obviously, these HAADF-STEM characterizations along the a and c axes reveal the 4 × 3 tunneled-structure of the NR, which was further corroborated by the cross-section observation viewed along the b axis of a NR in Fig. 1h. The cross-section samples were prepared elaborately using focused ion beam (FIB) cutting approach provided in Experiment Section. The magnified HAADF-STEM image in Fig. 1i clearly shows that the atomic structure consists of 4 × 3 tunnels where the bright spots surrounding each tunnel refer to MnO_6 atomic columns. This observation also matches well with the atomic model structure along the b axis in Fig. 1j. To the best of our knowledge, this is the first omni-directional atomic-resolution characterization of the τ-MnO_2 material.

The *in situ* electrochemical lithiation experiment is schematically illustrated in Fig. 2a and the detailed procedure can be found in Experiment Section. Real-time Li^+ transport pathways and morphological evolutions observed for two NRs were sampled by a series of still images shown in Fig. 2b − l (Movie S1 and S2, Supplementary material). Throughout the whole process, two distinct transport pathways of Li^+ are observed. First, transport of Li^+ in NR I propagated along the longitudinal direction starting from the point of contact with the metal Li tip. Upon applying the potential, an obvious reaction front (RF, marked by red arrows) appeared, specifically characterized by substantial cross-sectional expansion, and propagated longitudinally in Fig. 2c–f, while the region behind it underwent a 28.78% radial expansion (66–85 nm) accompanied by the appearance of numerous tiny crystallites. No fracture and cracking were observed in spite of substantial volume expansion upon lithiation. Such morphological changes were undoubtedly due to electrochemical lithiation rather than beam-induced phase decomposition, as evidenced by repeated careful *in situ* experiments (Fig. S2 and S3, Movie S3 and S4, Supplementary material).

Supplementary video related to this article can be found at https://doi.org/10.1016/j.nanoen.2019.06.036.

The lithiation RF longitudinally propagated ~125 nm within the first 20 s, corresponding to a speed of 6 nm s^{-1}. Within next 20 s, the RF moved only ~25 nm. The propagation distance of the RF as a function of time is plotted in Fig. S4 (Supplementary material). We believe that this nonuniform motion of the RF could be attributed to the gradually limited Li^+ transport on the surface of the NR, while the NR surface

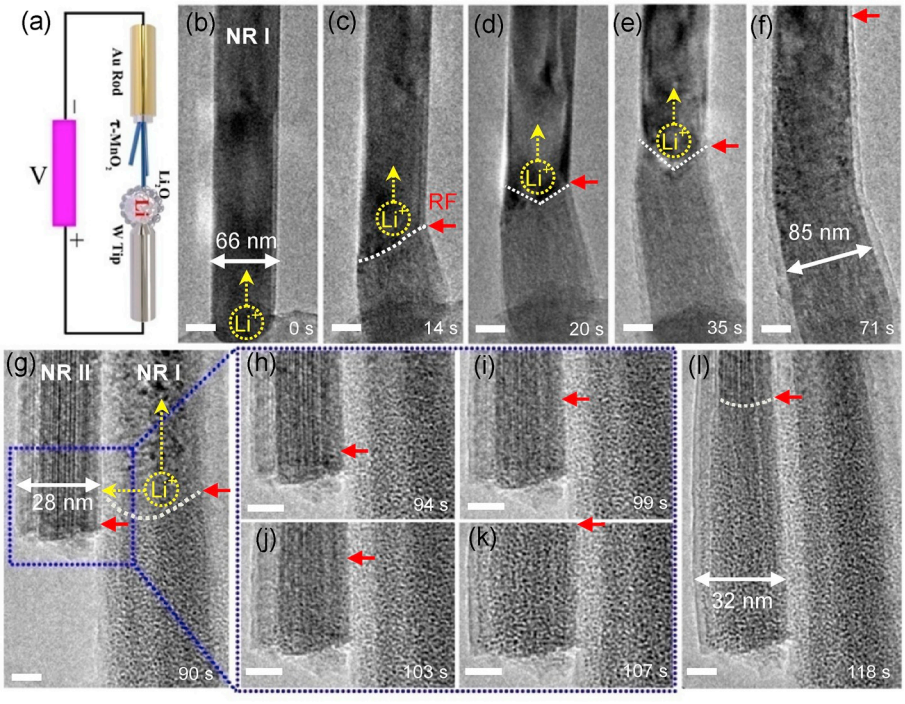

Fig. 2. *In situ* visualization of lithium-ion transport pathways. (a) Schematic illustration of the experiment setup. Electrochemical lithiation is initiated by applying a constant potential of −1.5 V to the NRs with respect to the Li counter electrode. (b–f) Snapshots of τ-MnO_2 NR during lithiation, showing the Li^+ transport pathway along b axis. The yellow arrows correspond to the Li diffusion direction. Scale bars, 30 nm. (b) Morphology before applying potential. (c–e) Propagation of the reaction front (RF, marked by red arrows) with considerable volume expansion. The V-shaped RF interface (marked by white dotted lines) proves the surface transport of Li^+ indirectly. (f) The final lithiated state featured by fully expanded NR I. (g–l) TEM projections of τ-MnO_2 NRs during lithiation, showing lateral Li-transport pathways between NRs. Yellow arrows show simultaneous lateral and longitudianal Li^+ transport pathways. (g) Pristine NR II attached to partially lithiated NR I due to oriented attachment growth mechanism. (h–k) The magnifying area of g marked by the blue dashed box show lithiation process in NR II through lateral contacts between NRs I and II. (l) Lithiated NR II and NR I. Scale bars, 10 nm.

near the Li^+ source was firstly wetted by a thin layer of lithium [36], thus facilitating the initial lithiation reaction. In addition, the V-shaped RF interfaces (marked by dotted lines) observed in Fig. 2c–f also proved the initial faster surface transport of Li^+ indirectly. Note that the wetting layer was so thin (< 5 nm) that the flux of Li^+ transported by this layer was outmatched by the flux from solid-state diffusion inside the NR. Thus, the surface transport of Li^+ was gradually restricted with increasing the transport length.

Starting at 90 s, the RF from NR I reached NR II where a second pathway for lithium transport was observed in Fig. 2g. In this scenario, the lithiation-induced expansion of NR I created close lateral contact points between both NRs. Therefore, the RF can cross their contact interface. The lithiation of NR II was none the less along its long axis, characterized by a newly emerged RF starting from the lower end of NR II, as shown in Fig. 2h–k (Movie S2, Supplementary material). This phenomenon seems to be slightly different from the lateral transfer of Li^+ in the case of 2 × 2 tunnel-structured α-MnO_2 NRs [37], in which the lithiation proceeded in both radial and longitudinal directions, away from the contact interface [38]. In particular, although the initial resource of Li^+ was different (lateral transfer), the resulting radial expansion of NR II was essentially the same as that observed in NR I. This lateral transfer of Li^+ from a prelithiated NR was further corroborated by additional *in situ* experiments in Fig. S5 and S6 (Movie S5 and S6, Supplementary material). Prelithiated NRs were used to laterally contact pristine NRs and the electrochemical lithiation was easily transferred to the pristine NRs, proving an unhindered lateral transport pathway between the NRs. The laterally lithiated NRs also exhibited the same radial expansion as that of NRs I and II in Fig. 2. The observation of the facile, local transfer of Li^+ between NRs in a localized contact region clearly indicated *ac* plane diffusion of Li^+ within the lithiated NRs.

Supplementary video related to this article can be found at https://doi.org/10.1016/j.nanoen.2019.06.036.

More in-depth understanding of the structural evolution during lithiation was used to explore the precise lithiation mechanism. A recorded movie of the *in situ* dynamic TEM lithiation progress of a NR is shown in Movie S7 (Supplementary material). Fig. 3a shows the clear lattice fringes of (001) plane viewed along the NR [100] zone axis. In Fig. 3b, the high-resolution snapshot of lithiation process from the movie shows two distinct regions observed: the α and β regions, separated by a RF (indicated by red arrow and white dashed line). For the β region, owing to a small amount of Li^+ intercalation, the tunneled structure was maintained basically, with a 4.7% expansion of the (001) lattice spacing. While in the α region, the full lithiation resulted in thorough collapse of the lattice, characterized by a substantial volume expansion and concomitant phase transformation. The fully lithiated NR was covered with tiny crystallites (marked with white circles). The real-time lithiation scenario can be schematically illustrated in Fig. 3c. Similar findings were also obtained in additional *in situ* lithiation experiments in Fig. S7a − c (Movie S8, Supplementary material).

Supplementary video related to this article can be found at https://doi.org/10.1016/j.nanoen.2019.06.036.

To further delineate the phase evolution of τ-MnO_2 NR during lithiation, we further analyzed the ED patterns corresponding to the regions marked in Fig. 3a and b. The ED pattern in Fig. 3d showed the pristine τ-MnO_2 structure oriented along the [100] zone axis. Upon initial lithiation, the ED pattern from the β region in Fig. 3e showed noticeable changes with diffraction spots beginning to elongate into circular arcs, but the todorokite structure was none the less well-preserved. The lattice change was measured from the diffraction spots, showing that the *b* and *c* values were expanded by 1.4% and 0.52%, respectively. Some diffraction spots attributable to Mn_2O_3 (JCPDS No.41–1442) and Mn (JCPDS No.33–0887) developed, although their intensities were a little weak. As shown in Fig. 3f, the ED pattern from the RF showed both Mn and Mn_2O_3 diffraction spots, and the ED pattern belonging to the τ-MnO_2 structure disappeared completely. After full lithiation, the ED pattern from the α region in Fig. 3g, showed discrete diffraction rings of only Mn and Li_2O phases, revealing metal Mn as the fully lithiated product. The observed lattice expansion and intermediate phase Mn_2O_3 were also observed in additional cases in Fig. S7 (Supplementary material). Therefore, an intercalation-conversion reaction mechanism can be identified: Li^+ firstly intercalated into the tunneled structure of τ-MnO_2 and then reacted with this material, forming intermediate phase Mn_2O_3 that was ultimately reduced to Mn crystallites dispersed into Li_2O matrix.

To better understand the phase evolution, we performed local EELS measurements from the *in situ* lithiated NR in the order of lithium concentration, as shown in Fig. 3h and i. The increased intensity of Li–K edge and the shift of Mn-$M_{2,3}$ edge are clearly observed as the lithiation progressed in Fig. 3h. The integral intensity ratio of the Mn L_3 ($2p_{3/2}\rightarrow 3d$) and L_2 ($2p_{1/2}\rightarrow 3d$) edges of each spectrum was calculated based on Pearson method with double step functions to evaluate the change in the valence states [39,40]. In Fig. 3j, the Mn L_3/L_2 intensity ratio increases at higher lithiation levels up to the spectrum labeled "viii", due to the decreased Mn oxidation state [41–43]. In particular, the intensity ratio was calculated to be 2.6 for the spectrum "v", strongly supporting the formation of the Mn_2O_3 intermediate phase and the beginning of the conversion reaction. Moreover, we also observed three splitting peaks (a_1, a_2, and a_3) in the prepeak regions of the spectra "iv" and "v", as inserted in Fig. 3i. According to the molecular-orbital calculation, the triply peaked structure is characteristic of Mn_2O_3, attributable to the transition to $3e_g\uparrow$, $2t_{2g}\downarrow$, and $3e_g\downarrow$ unoccupied states, respectively [44]. However, the Mn L_3/L_2 intensity ratio begins to decrease after the spectrum "viii". A lower L_3/L_2 intensity ratio for Mn metal than for the Mn_2O_3 phase would contribute to this switch [39,44], implying that the Mn metal phase began to form as a result of the final conversion reaction in which the Mn_2O_3 intermediate phase was converted into Mn metal and Li_2O phases [45,46].

DFT calculations, described in Experiment Section, were used to better comprehend the local atomic structure associated with each phase. In Fig. 4a, the intergrowth structure of two 4 × 3 tunnels along the *b* axis of τ-MnO_2 was modeled based on lattice constants of $a = 23.20$ Å, $b = 5.36$ Å, $c = 9.14$ Å, and $\beta = 99.66°$. For more precise analysis, the tunnel stabilizers such as Mg^{2+} and H_2O have been included in the unit cell [47,48], despite considerably heavy computational workload. Initially, the Li ions were inserted into the unoccupied sites inside the tunnels, causing a slight tunnel distortion along the *c* direction, as illustrated by the stable phases ($x = 0.29$, 0.57 and 1 Li per MnO_2) in Fig. S8 (Supplementary material). The Li ions in the tunnels formed electrovalent bonds with oxygen, as displayed by electron localization functions (ELF) in Fig. S9 (Supplementary material). At this moment, the Li transport was basically restricted within the distorted tunnels due to the still unbroken MnO_6 octahedra tunnel walls, even at a higher Li^+ concentration of 1.43 in Fig. 4b. This lithiation stage corresponds to the intercalation reaction coincident with slightly increased lattice constants, as reflected by 2–10% radial expansion in the β region of a lithiating NR oriented along its *a* axis, as shown in Fig. 4e. In addition, the slight contrast change in the β region was distinguishable in the TEM bright-field image in Fig. 4e (Movie S7, Supplementary material), indicating an initial phase segregation of Mn_2O_3 and Mn phases ahead of the full conversion reaction.

As the Li^+ concentration increased to $x = 2.21$, the tunnel walls began to disrupt as a result of large lattice expansion along the *a* and *c* directions (11.7% and 14.2% in Table S1, Supplementary material), as shown in Fig. 4c. This disruption would facilitate rapid lateral ($a-c$ plane) diffusion of lithium between NRs as well as within NRs, as observed *in situ* in Fig. 2g − l. This stage was characterized by internal disorder in which the lattice fringes gradually vanished, corresponding to the RF in Fig. 4e. Undoubtedly, the conversion reaction had occurred at this lithiation level, as validated by ED pattern in Fig. 3f. For higher Li^+ concentration ($x = 3.93$), the wall structure fully opened and the cell cross section area was substantially increased coincident with further lattice expansion up to 27.8 and 25.3% along the *a* and *c* directions, respectively, in Fig. 4d. The conversion reaction dominated the α region with final Mn and Li_2O phases, as

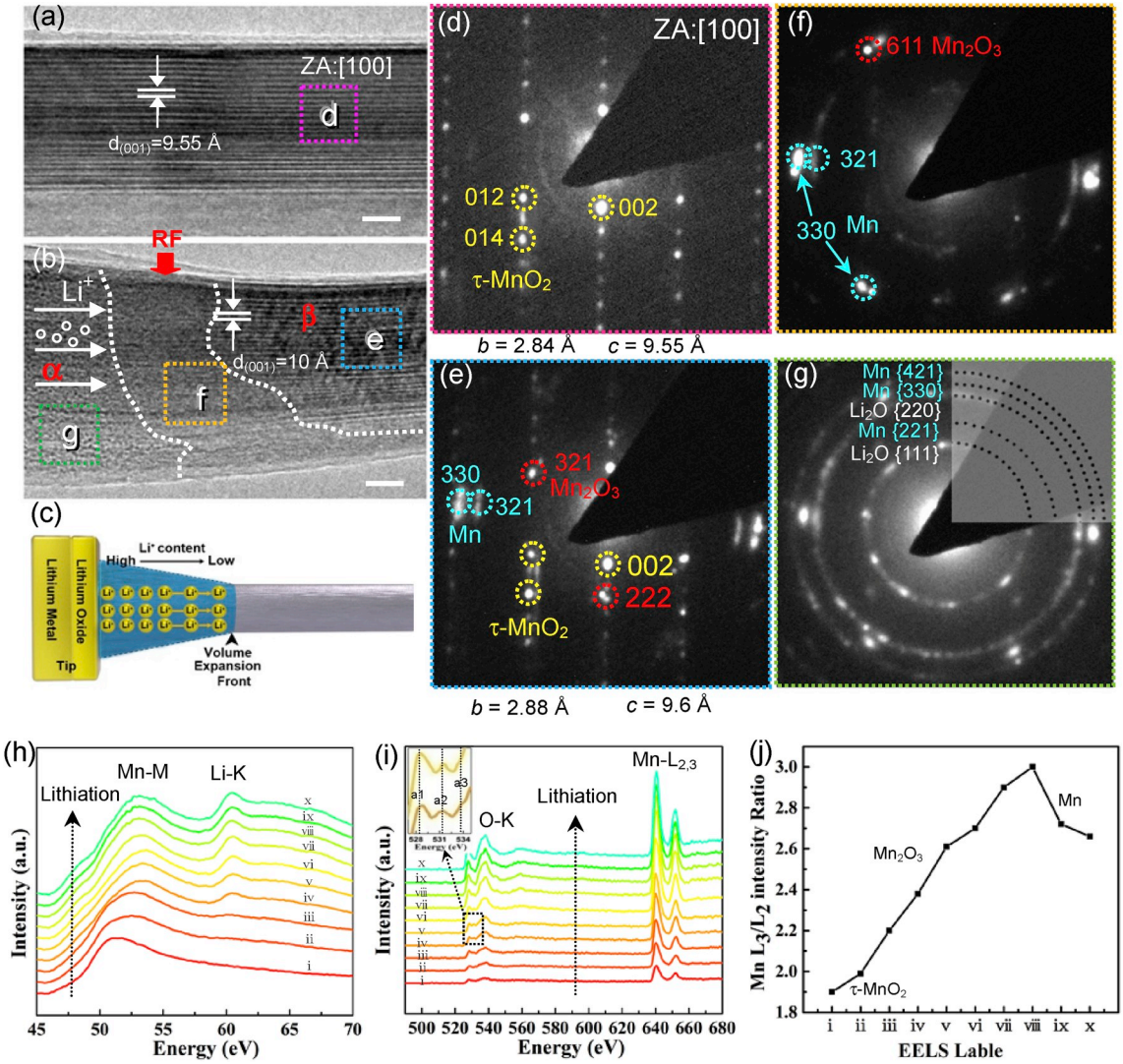

Fig. 3. Lattice-resolution structural evolution during lithiation. (a) [100] HRTEM image of a pristine τ-MnO_2 NR. Scale bar, 10 nm. (b) [100] HRTEM image of a partially lithiated τ-MnO_2 NR. The white arrows correspond to Li diffusion direction. The red arrow and white dashed line represent RF. Two regions with different characteristics are defined: region α is lithiated section covered with many tiny crystallites (white circles); region β represents lithium intercalation, in which the lattice of (001) expanded from 9.55 Å to 10 Å. Scale bar, 10 nm. (c) Schematic illustration of a partially lithiated NR. (d–g) ED patterns collected from dashed box in a and b, showing the structural evolutions during lithiation. (d) ED pattern shows monocrystalline structure of the NR. (e) ED pattern for β region shows tunnels still preserve at initial lithiation stage. New spots of Mn_2O_3 emerge (marked by red circles), indicating reduction of Mn^{4+} to Mn^{3+}. The existence of metal Mn spots (marked by blue circles) suggests the formation of Mn crystallites. Below shows the lattice parameters of the τ-MnO_2 NR calculated from the ED pattern. (f) ED pattern for RF region. Diffraction spots of τ-MnO_2disappear and those of Mn phase are strengthen with brighter spots for Mn (321). Note that Mn_2O_3 phase still exists (red circle). (g) ED pattern for α region, revealing the lithiation product is metal Mn, evolved from Mn_2O_3. (h–j) Arranged STEM-EELS data in the order of Li^+ concentration, collected from lithiated NRs. (h) Mn-M and Li–K edges. (i) O–K and Mn-L edges. Inset refers to three splitting peaks (a_1, a_2, and a_3) in the prepeak region of the spectra "iv" and "v", indicating the formation of Mn_2O_3 phase. (j) Intensity ratio of Mn-L_3/L_2 edge in i.

demonstrated by the EELS and ED patterns in Fig. 3g−j. Furthermore, we also measured a 27.3% *b*-axis (or longitudinal) elongation after full lithiation of a NR in Fig. S10 (Movie S9, Supplementary material). This value is consistent with the calculation result (27.6%) of *b*-lattice expansion after inserting 3.93 Li ions.

Supplementary video related to this article can be found at https://doi.org/10.1016/j.nanoen.2019.06.036.

The lithiated products associated with phase transformations were further delineated using the bader charge analysis [49,50], in Fig. S11 (Supplementary material). In τ-MnO_2, Mn can be considered as a positive center with +1.64 e, whereas O can be a negative center with −1.64 e. Blue and green stars represent the average bader charges of Mn in manganese metal and Li in Li_2O, respectively. The charge of +1.64 e for Mn ions drastically descended with increasing Li concentration until the charge decreased to 0 e for the formation of Mn cluster. In the meantime, the charge for Li ions dropped to +0.79 e for the formation of Li_2O. The calculated energies here indicate that the phase transformation during lithiation is driven by entropy reduction force. According to the aforementioned results, we can conclude that during the full lithiation process of τ-MnO_2, the lithium ions first intercalate into τ-MnO_2 NR under a suitable potential and then react with τ-MnO_2, forming the intermediate product of Mn_2O_3, which are further reduced to Mn crystallites dispersed in the Li_2O matrix. The stepwise intercalation-conversion lithiation mechanism suggested here can be expressed as follows:

$$MnO_2 + xLi^+ + xe^- \rightarrow Li_xMnO_2 \quad (5)$$

$$2Li_xMnO_2 + (2-2x)Li^+ + (2-2x)e^- \rightarrow Mn_2O_3 + Li_2O \quad (6)$$

$$Mn_2O_3 + 6Li^+ + 6e^- \rightarrow 2Mn + 3Li_2O \quad (7)$$

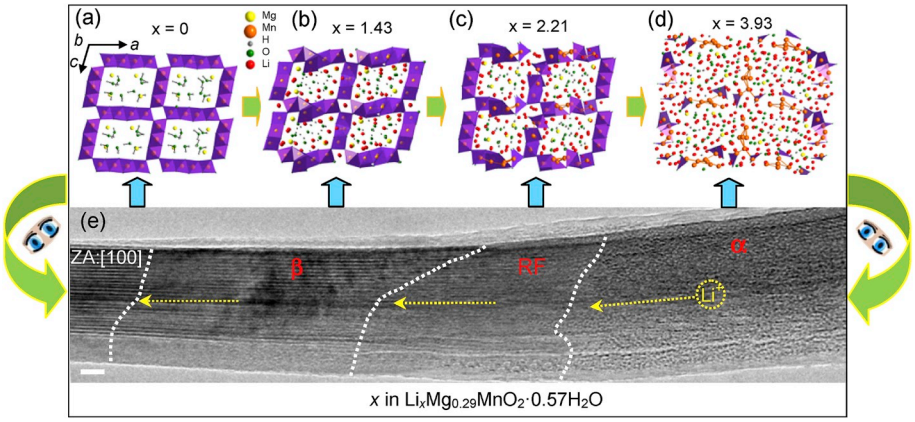

Fig. 4. Atomic-scale DFT calculations associated with lithiation levels. (a) The intergrowth structure of four 4 × 3 tunnels along the b axis. Electrochemical lithiation process of τ-MnO_2 NR start from the modeled structure (x = 0). The Li atoms insert into the unoccupied sites of the tunnels for a range of compositions with $0 < x < 4$ for $Li_xMg_{0.29}MnO_2{\cdot}0.57H_2O$. (b) $Li_{1.43}Mg_{0.29}MnO_2{\cdot}0.57H_2O$ phase. The Li transport is still restricted inside the distorted tunnels at this moment due to the unbroken MnO_6 octahedra tunnel walls. (c) $Li_{2.21}Mg_{0.29}MnO_2{\cdot}0.57H_2O$ phase, presenting opened and partially disrupted tunnel walls, which would facilitate rapid lateral (a − c plane) diffusion of lithium between NRs as well as within NRs. (d) High Li concentration phases ($Li_{3.93}Mg_{0.29}MnO_2{\cdot}0.57H_2O$), exhibiting complete disruption of the tunnel walls and being calculated to phase segregation. (e) [100] HRTEM image of a partially lithiated τ-MnO_2 NR. The yellow arrows correspond to the Li diffusion direction. Scale bar, 5 nm.

Further, the cyclic voltammetry (CV) test at scan rate of 0.1 mV s^{-1} was performed to delineate the lithiation mechanisms of τ-MnO_2 material, as shown in Fig. 5a. The three reaction regions labeled as I, II, and III are distinct in the CV curves. In the region I, no intense cathodic peaks appear and the intercalation reaction should dominate this stage. Following this initial lithiation, a two-step conversion reaction could take place in the region II involving the formation of intermediate Mn_2O_3 phase and in the region III corresponding to the phase conversion from Mn_2O_3 to Mn. Fig. 5b shows the discharge-charge profile acquired with a current rate of 0.1 A g^{-1} between 0.01 V and 4 V (vs Li/Li^+), which also reflects the same three reaction regions as those in Fig. 5a. It can be seen from the discharge-charge profile that the specific capacities of 150 mAh g^{-1} and 980 mAh g^{-1} respectively corresponding to the intercalation reaction and conversion reaction can be achieved.

Undoubtedly, exploring the full lithiation process makes sense. Further, understanding reversible delithiation process is significant as much, considering potential application of this material for rechargeable batteries. In like manner, we traced structural evolutions during the *in situ* delithiation process of a prelithiated NR in Fig. 6a–d (Movie S10, Supplementary material). Unexpectedly, we for the first time observed the reciprocating motion of a delithiation RF (DRF) within single nanomaterials. Different from the one-way motion of the LRF, the extraction of Li^+ upon delithiation is characterized by the round-trip DRF, indicating a two-stage delithiation mechanism. After applying a reversed biasing, a DRF (denoted by green arrow) first started from the NR end near the Li source and gradually propagated along the NR to another end in Fig. 6a. As a result, the NR exhibited a visible decrease in diameter from 59 nm to 57 nm, accompanied with a slight change in the interior contrast of the NR. During this stage, we notice that the initially formed LRF basically kept immobile, implying an incomplete lithium extraction.

Supplementary video related to this article can be found at https://doi.org/10.1016/j.nanoen.2019.06.036.

Impressively, the immobile LRF seemed to be activated when the DRF approached it. Apparently, the DRF devoured the LRF and then returned back to its starting point immediately, further causing substantial cross-section contraction until ~53 nm in diameter, as shown in Fig. 6d. At this stage, we clearly observed the contrast changes within the NR where the dark glossy region gradually became dominant. After the full delithiation, the ED pattern and EELS data show that only Mn_2O_3 phase was formed instead of the original τ-MnO_2 phase in Fig. 6b and c. To this extent, we think that one whole cycle of *in situ* lithiation-delithiation has been completed. To the best of our knowledge, this is the first report of a reciprocating-motion DRF associated with two delithiation stages (or levels). The DRF occurring in the second stage has been frequently observed in previous works, but little is known about the first stage. Considering the Mn_2O_3 phase as the only delithiated product and no intermediate phase during delithiation, we therefore assume the first stage as the pre-nucleation stage of the Mn_2O_3 phase. Due to the partial deinsertion of Li^+ from Li_2O, the activated O was generated and subsequently combined with Mn to form the Mn_2O_3 phase, due to the favorable binding energy of −2.024 eV between O and Mn for Mn_2O_3 phase.

To provide more insights into our conjecture and the experimentally observed (de)lithiation behaviors, we employed a phase field model to delineate the driven dynamics of the Li^+ concentration inside the material via the Cahn-Hilliard equation, an internal free energy functional, and boundary conditions for the electrochemical interface derived from the Butler-Volmer equation [51]. For modelling purposes, we assumed the material had a stable phase for Li concentrations of $x = 0$, 0.5 and

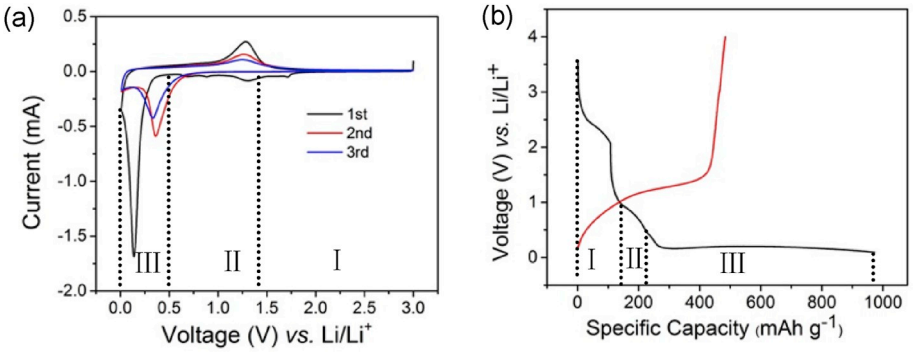

Fig. 5. Electrochemical performance of τ-MnO_2 electrode in lithium-ion battery. (a) CV curves recorded at a sweep rate of 0.1 mV s^{-1}. (b) Discharge-charge profile was acquired with the current rate of 0.1 A g^{-1} between 0.01 V and 4 V (vs Li/Li^+).

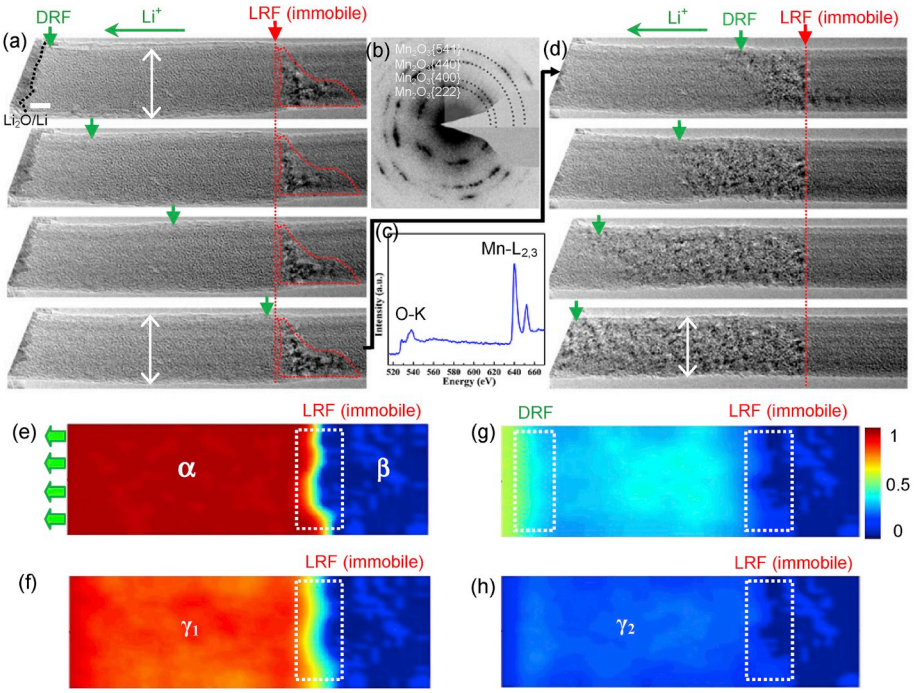

Fig. 6. *In situ* visualization of reciprocating motion of a delithiation RF (DRF) and structural evolutions upon delithiation. (a) Experimental snap shots from *in situ* delithiation process of pre-lithiated τ-MnO_2 NR, showing that DRFs denoted by green arrows emerge and gradually propagate from the side approaching the Li source to the another. (b) ED pattern of delithiation product. (c) EELS spectrum of delithiation product. (d) TEM images from the second stage of delithiation, showing that DRFs propagate in the opposite direction. (e–h) Snap shots from two-dimensional phase-field simulation illustrate dynamical phase evolutions during delithiation. (e) High lithiation state. Two-dimensional maps with the color legend indicate normalized Li concentration and three distinct regions: the LRF, the area in front of the LRF (α), and behind (β). The α area is assumed to have Li concentration of $x = 1$. (f) Low-level delithiation phase γ_1, in which the initial LRF stands still. (g,h) The DRF moved down the NR, with γ_2 phase formation and coarsening. Scale bars, 10 nm.

1. The dynamic simulation of lithiation was illustrated in Fig. S12a−f (Movie S11, Supplementary material). For the delithiation process, we started with the final lithiation influx of Li^+ which had reached an average concentration $x = 1$ and simulated the evolution of system on the time scale characterized by the DRF motion in Fig. 6e (Movie S12, Supplementary material). Model parameters, carefully chosen to qualitatively capture the region observed experimentally, are listed in Table S2 (Supplementary material).

Supplementary video related to this article can be found at https://doi.org/10.1016/j.nanoen.2019.06.036.

We first observed that the low Li concentration (x~0.8, γ_1 phase) emerged because of partial extraction of Li^+, but the initial LRF still stood still in Fig. 6f. As the delithiation continued, the DRF moved down the NR, shrinking the volume of the γ_2 phase in Fig. 6g and h. Our simulations also indicated that the details of microstructure evolution were sensitive to the coefficients in the free energy function. The γ_1 and γ_2 depended on the energy barrier between the two phases. The simulations presented in Fig. 6e−h exhibit the balance between the time scale associated to the γ_1 phase emerging, the γ_2 phase coarsening, and the DRF motion, consistent with the experimental observations in Fig. 6a−d. Additionally, during subsequent lithiation and delithiation cycles in Fig. S13 (Movie S13, Supplementary material), a stable and reversible phase transformation between Mn_2O_3 and Mn + Li_2O phases would be established, as evidenced by the ED results in Fig. S13k,l (Supplementary material).

Supplementary video related to this article can be found at https://doi.org/10.1016/j.nanoen.2019.06.036.

4. Conclusion

In summary, we have successfully attempted to synthesize relatively pure 4 × 3 tunnel-structured τ-MnO_2 NRs confirmed via atomically resolved imaging. A comprehensive study of the (de)lithiation process of the τ-MnO_2 NRs has been conducted using the *in situ* TEM, revealing a stepwise intercalation-conversion lithiation mechanism. By combining the *in situ* HRTEM imaging, ED, EEL spectroscopy, and DFT calculations, we first traced the entire reaction procedure up to full lithiation levels in NRs. The intercalation reaction occurred in early lithiation stage with the tunnel distortion and the radial ($a-c$ plane) expansion. Subsequently, the conversion reaction began, which finally formed Mn metal and Li_2O phases through an Mn_2O_3 intermediate phase. Meanwhile, the tunnel walls were disrupted, enabling two distinct lithium transport pathways including lateral inter-rod and axial intra-rod lithiations. In contrast to the unidirectional lithiation RF, we observed an unusual reciprocating-motion delithiation RF, for which the driven dynamics involving the lithium concentration are revealed by employing a phase field model. Notably, this is the first time-resolved visualization of the reciprocating-motion delithiation RF, suggesting two distinct delithiation stages (or levels). This work has supplied the in-depth understanding of precise (de)lithiation mechanism of the 4 × 3 tunnel-structured τ-MnO_2 and provided an important new context for understanding of kinetic limitations for lithium transport in 1D materials, including materials structurally and compositionally related to the todorokite-type material. Additionally, this work is also expected to provide a paradigm shift for other tunnel-specific phases of the τ-MnO_2 for establishing more precise structure-property relation.

Acknowledgements

This work was supported by the National Natural Science Foundation of China (Grant Nos. 11774051, 61574034, 11525415, 51420105003, 11774052), the 973 Program (Grant No. 2015CB352106), the National Key R&D Program of China (Grant Nos. 2016YFA0300804, 2016YFA0300903), National Equipment Program of China (ZDYZ2015-1), China Postdoctoral Science Foundation Funded Project (2014M550259, 2015T80480), Jiangsu Planned Projects for Postdoctoral Research Funds (1401006A), and the Fundamental Research Funds for the Central Universities (2242018K41020). The authors acknowledge the Electron Microscopy Laboratory in Peking University for the use of *in situ* TEM platform.

R.C. and F.X. were inspired by two valuable papers (Science, 1981, 212, 1024; RSC Advances, 2015, 5, 106265) and then synthesized the bulk material independently in Southeast University using a newly modified method. R.C. and F.X. conducted all *in situ* experiments in Southeast University and Peking University, respectively. P.G., M.L. and Y.S. characterized the atomic structure of nanorod sides via the scanning transmission electron microscopy with a high-angle annular dark field detector in Peking University. K.K. prepared the cross-section

samples of nanorods that were subsequently characterized by H.X. and S.Y. at Brookhaven National Laboratory. R.C., P.G., M.L. and Y.S. collected electron energy-loss spectroscopy in Peking University. S.Z, S.G., and H.Z. completed the density functional theory calculations. The phase field model was done by Q.M. and Y.Z. at Brookhaven National Laboratory. R.C., F.X., P.G., S.Z., X.H., H.D. and S.L. carried out the data analysis. F.X. and L.S. directed this work. All authors contributed to writing and revision of the manuscript.

Appendix A. Supplementary data

Supplementary data related to this article can be found at https://doi.org/10.1016/j.nanoen.2019.06.036.

References

[1] P. Canepa, G.S. Gautam, D.C. Hannah, R. Malik, M. Liu, K.G. Gallagher, K.A. Persson, G. Ceder, Chem. Rev. 117 (2017) 4287–4341.
[2] D.M. Robinson, Y.B. Go, M. Mui, G. Gardner, Z.J. Zhang, D. Mastrogiovanni, E. Garfunkel, J. Li, M. Greenblatt, G.C. Dismukes, J. Am. Chem. Soc. 135 (2013) 3494–3501.
[3] J. Zhang, Y. Shi, Y. Ding, W.K. Zhang, G.H. Yu, Nano Lett. 16 (2016) 7276–7281.
[4] S.W. Zhang, Q.H. Fan, H.H. Gao, Y.S. Huang, X. Liu, J.X. Li, X.J. Xu, X.K. Wang, J. Mater. Chem. A 4 (2016) 1414–1422.
[5] A.S. Poyraza, J.P. Huang, S.B. Cheng, L.J. Wu, X. Tong, Y.M. Zhu, A.C. Marschilok, K.J. Takeuchi, E.S. Takeuchi, J. Electrochem. Soc. 164 (2017) 1983–1990.
[6] Y. Liu, P.Y. Zhang, Appl. Catal. A: Gen. 530 (2017) 102–110.
[7] Y.F. Yuan, L. Ma, K. He, W.T. Yao, A.M. Nie, X.X. Bi, K. Amine, T.P. Wu, J. Lu, R. Shahbazian-Yassr, Nano Energy 19 (2016) 382–390.
[8] S.Y. Lee, L.J. Wu, A.S. Poyraz, J.P. Huang, A.C. Marschilok, K.J. Takeuchi, E.S. Takeuchi, M. Kim, Y.M. Zhu, Adv. Mater. 29 (2017) 1703186.
[9] L.H. Li, C.Y. Nan, J. Lu, Q. Peng, Y.D. Li, Chem. Commun. 48 (2012) 6945–6947.
[10] Y. Yang, D. Shu, J.K. You, Z.G. Lin, J. Power Sources 81–82 (1999) 637–641.
[11] E. Sahadeo, J. Song, K. Gaskell, N. Kim, G. Rubloff, S.B. Lee, Phys. Chem. Chem. Phys. 20 (2018) 2517–2526.
[12] S. Rosenberg, A. Hintennach, J. Power Sources 274 (2015) 1043–1048.
[13] D.A. Tompsett, S.C. Parker, M. Saiful Islam, J. Mater. Chem. A 2 (2014) 15509–15518.
[14] J. Ostwald, Mineral. Mag. 50 (1986) 336–340.
[15] X.B. Hu, D.A. Kitchaev, L.J. Wu, B.J. Zhang, Q.P. Meng, A.S. Poyraz, A.C. Marschilok, E.S. Takeuchi, K.J. Takeuchi, G. Ceder, Y.M. Zhu, J. Am. Chem. Soc. 140 (2018) 6961–6968.
[16] N. Kumagai, S. Komaba, K. Abe, H. Yashiro, J. Power Sources 146 (2005) 310–314.
[17] J.E. Post, D.L. Bish, Am. Mineral. 73 (1988) 861–869.
[18] Y.F. Yuan, A.M. Nie, G.M. Odegard, R. Xu, D.H. Zhou, S. Santhanagopalan, K. He, H. Asayesh-Ardakani, D.D. Meng, R.F. Klie, C. Johnson, J. Lu, R. Shahbazian-Yassar, Nano Lett. 15 (2015) 2998–3007.
[19] M.J. Duncan, F. Leroux, J.M. Corbett, L.F. Nazar, J. Electrochem. Soc. 145 (1998) 3746–3757.
[20] Y.F. Yuan, C. Liu, B.W. Byles, W.T. Yao, B.A. Song, M. Cheng, Z.N. Huang, K. Amine, E. Pomerantseva, R. Shahbazian-Yassar, J. Lu, Joule 3 (2019) 1–14.
[21] Y.F. Li, S.C. Zhu, Z.P. Liu, J. Am. Chem. Soc. 138 (2016) 5371–5379.
[22] Y.F. Shen, R.P. Zerger, R.N. DeGuzman, S.L. Suib, L. McCurdy, D.I. Potter, C.L. O'Young, Science 260 (1993) 511–515.
[23] B.W. Byles, D.A. Cullen, K.L. More, E. Pomerantseva, Nano Energy 44 (2018) 476–488.
[24] B. Lan, L. Yu, T. Lin, G. Cheng, M. Sun, F. Ye, Q.F. Sun, J. He, ACS Appl. Mater. Interfaces 5 (2013) 7458–7464.
[25] J.P. Perdew, K. Burke, M. Ernzerhof, Phys. Rev. Lett. 77 (1996) 3865–3868.
[26] G. Kresse, J. Hafner, Phys. Rev. B: Condens. Matter 7 (1993) 558–561.
[27] P.E. Blöchl, Phys. Rev. B 50 (1994) 17953.
[28] V.I. Anisimov, F. Aryasetiawan, A.I. Lichtenstein, J. Phys. Condens. Matter 9 (1997) 767–808.
[29] F. Zhou, M. Cococcioni, C.A. Marianetti, D. Morgan, G. Ceder, Phys. Rev. B 70 (2004) 235121.
[30] D.A. Tompsett, M.S. Islam, Chem. Mater. 25 (2013) 2515–2526.
[31] M.Z. Bazant, Acc. Chem. Res. 46 (2013) 1144–1160.
[32] P. Bai, D.A. Cogswell, M.Z. Bazant, Nano Lett. 11 (2011) 4890–4896.
[33] M. Tang, W.C. Carter, Y.-M. Chiang, Annu. Rev. Mater. Res. 40 (2010) 501–529.
[34] B.W. Byles, P. West, D.A. Cullen, K.L. More, E. Pomerantseva, RSC Adv. 5 (2015) 106265–106271.
[35] Q. Feng, H. Kanoh, Y. Miyai, K. Ooi, Chem. Mater. 7 (1995) 1722–1727.
[36] W.W. Xia, F. Xu, C.Y. Zhu, H.L. Xin, Q.Y. Xu, P.P. Sun, L.T. Sun, Nano Energy 27 (2016) 447–456.
[37] F. Xu, L.J. Wu, Q.P. Meng, M. Kaltak, J.P. Huang, J.L. Durham, M. Fernandez-Serra, L.T. Sun, A.C. Marschilok, E.S. Takeuchi, K.J. Takeuchi, M.S. Hybertsen, Y.M. Zhu, Nat. Commun. 8 (2017) 15400.
[38] L.J. Wu, F. Xu, Y.M. Zhu, A.B. Brady, J.P. Huang, J.L. Durham, E. Dooryhee, A.C. Marschilok, E.S. Takeuchi, K.J. Takeuchi, ACS Nano 9 (2015) 8430–8439.
[39] H.Y. Tan, J. Verbeeck, A. Abakumov, G.V. Tendeloo, Ultramicroscopy 116 (2012) 24–33.
[40] X. Li, X.H. Ma, D. Su, L. Liu, R. Chisnell, S.P. Ong, H.L. Chen, A. Toumar, J. Idrobo, Y.C. Lei, J.M. Bai, F. Wang, J.W. Lynn, Y.S. Lee, G. Ceder, Nat. Mater. 13 (2014) 586–592.
[41] F. Wu, G.X. Yu, D. Xu, E. Kan, J. Phys. Condens. Matter 24 (2012) 456002.
[42] D.H. Pearson, C.C. Ahn, B. Fultz, Phys. Rev. B 47 (1993) 8471–8478.
[43] J.H. Paterson, O.L. Krivanek, Ultramicroscopy 32 (1990) 319–325.
[44] H.K. Schmid, W. Mader, Micron 37 (2006) 426–432.
[45] L.A.J. Garvie, A.J. Craven, Phys. Chem. Miner. 21 (1994) 191–206.
[46] H. Kurata, C. Colliex, Phys. Rev. B 48 (1993) 2102–2108.
[47] A.L. Atkins, S. Shaw, C.L. Peacock, Geochim. Cosmochim. Acta 144 (2014) 109–125.
[48] S. Bodeï, A. Manceau, N. Geoffroy, A. Baronnet, M. Buatier, Acta 71 (2007) 5698–5716.
[49] R.F.W. Bader, Chem. Rev. 91 (1991) 893–928.
[50] C. Ling, D. Banerjee, W. Song, M.J. Zhang, M. Matsui, J. Mater. Chem. 22 (2012) 13517.
[51] J.W. Cahn, J.E. Hilliard, J. Chem. Phys. 28 (1958) 258–267.

Ran Cai is now a Ph.D. candidate at Key laboratory of MEMS of Ministry of Education, Southeast University, Nanjing, China. She received her Bachelor's degree and Master's degree from Nanjing University of Posts and Telecommunications in 2013 and 2016, respectively. Her research interests focus on the *in situ* TEM observation of electrochemical behaviors of nanomaterials.

Shiying Guo is now a Ph.D. candidate at MIIT Key Laboratory of Advanced Display Materials and Devices. She received her bachelor degree in Materials Science and Engineering from Nanjing University of Science and Technology in2016. Her current research interests are concentrated on exploring the 2D material application in optoelectronics and energy devices.

Dr. Qingping Meng is a visiting scientist in Condensed Matter Physics & Materials Science Department, Brookhaven National Laboratory, Upton, NY 11973-5000, USA. Qingping Meng is currently a visiting scientist in Brookhaven National Laboratory. He got his Ph.D. from Shanghai Jiao Tong University and then was promoted to Associate Professor at Shanghai Jiao Tong University in 2002. His research interests cover phase transformation in solids, thermal conductivity of thermo- electric materials, and Li-ion battery.

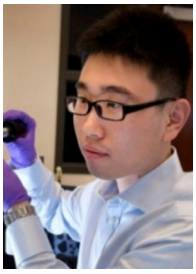

Dr. Huolin L. Xin is now an Associate Professor Department of Physics and Astronomy, University of California, Irvine, California, U.S.A. He received his Bachelor's degree from Peking University in 2005 and Ph.D. from Cornell University in 2011, respectively. He was a post-doctoral fellow in Lawrence Berkeley National Laboratory (2011–2013) and a staff material scientist in Brookhaven National Laboratory (2013–2018).He is interested in developing novel 3-D, atomic-resolution, *in situ* spectroscopic and imaging tools to probe the structural, chemical, and bonding changes of energy materials.

Mingqiang Li is now a Ph.D. candidate at Electron Microscopy Laboratory of Peking University, Beijing, China. He received his Bachelor's degree from Zhengzhou University in 2016. His research interests focus on the *in situ* TEM observation and atomic structure characterization of ferroelectric materials.

Yuanwei Sun is currently a Ph.D. candidate at the Electron Microscopy Laboratory and International Center for Quantum Materials, School of physics, Peking University, Beijing, China. He received his Bachelor's and Master's degree from Liaocheng University in 2013 and 2017, respectively. His research interests focus on characterization of ferroelectric materials by transmission electron microscopy (TEM) techniques.

Dr. Peng Gao is currently a Professor in School of Physics, Peking University, Beijing, China. He received his Ph.D. degree in 2010 from the Institute of Physics, Chinese Academy of Sciences. He was a post-doctoral fellow in University of Michigan (2010–2013), a research associate in Brookhaven National Laboratory (2013–2014), and a research fellow in in University of Tokyo (2014–2015). He was selected in Project of Thousand Youth Talents and then joined in Peking University in 2015. His research interests include electron microscopy, ferroelectrics, solid-state ionics, and structure and properties of crystal defects and interfaces.

Dr. Shengli Zhang received his Ph.D. degree from Beijing University of Chemical Technology in 2013. He then joined the Key Laboratory of Advanced Display Materials and Devices, Nanjing University of Science and Technology, where he is a Professor in the Department of Materials Science and Engineering. His research interests are focused on electronic or optoelectronic devices and applications based on 2D materials.

Dr. Hui Dong is currently working at Key Laboratory of Welding Robot and Application Technology of Hunan Province, Xiangtan University, Hunan province, China. He obtained his Ph.D. in 2018 from Southeast University. He was a Visiting Scholar at the Queensland University of Technology from 2016 to 2017. Currently, he concentrates on *in situ* Transmission and Scanning electron microscopy study on morphology and structure property relationship of nanomaterials, under multi field coupling including force, heat, optical, electric fields and so on.

Dr. Shuangying Lei is an Associate Professor in the Key Laboratory of MEMS of the Ministry of Education at Southeast University (SEU), Nanjing, China. She obtained her Ph.D. in 2006 from Peking University and was promoted to an Associate Professor in 2009, respectively. She was a Visiting Scholar in Rensselaer Polytechnic Institute from 2014 to 2015.Currently, she mainly employs density functional theory calculations to study structure-property relationship of nanomaterials.

Dr. Haibo Zeng received his Ph.D. from the Institute of Solid State Physics, Chinese Academy of Sciences, in 2006. He worked with Prof. Claus Klingshirn in 2007 at the University of Karlsruhe, Germany. In 2008, he joined Prof. Yoshio Bando's group at the National Institute for Materials Science, Japan, under the support of JSPS. In 2011, he returned to Nanjing University of Aeronautics and Astronautics as a full professor, and then moved to Nanjing University of Science and Technology in 2013 as a director of the Institute of Optoelectronics & Nanomaterials. His current research interest includes 2D materials and QDs.

Dr. Litao Sun is currently a Distinguished Professor at Southeast University, Nanjing, China. He received his Ph.D. from the Shanghai Institute of Applied Physics, Chinese Academy of Sciences, followed by postdoctoral research at University of Mainz, Germany and a visiting professorship at the University of Strasbourg, France. His current research interests include *in situ* experimentation inside the electron microscope, graphene and related 2D materials, new phenomena from sub-10 nm nanoparticles, and applications of nanomaterials in environment, energy, and nanoelectromechanical systems.

Dr. Feng Xu is a Professor in the Key Laboratory of MEMS of the Ministry of Education, Southeast University (SEU), Nanjing, China. He obtained his Ph.D. in 2009 from Nanjing Tech University. In 2012 and 2017, he was promoted to Associate Professor and Professor, respectively. He was a Visiting Scholar at Brookhaven National Laboratory from 2014 to 2015. Currently, he concentrates on study of structure-property relationship of nanomaterials, including but not limited to energy conversion and storage materials, by using *in situ* transmission electron microscopy.

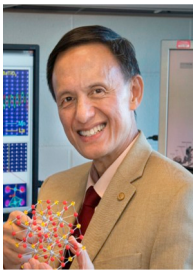

Dr. Yimei Zhu is a Senior Physicist in Condensed Matter Physics and Materials Science Department at Brookhaven National Laboratory, and an Adjunct Professor at Columbia University and at Stony Brook University in Stony Brook, New York. As one of the three Principal Investigators of the BNL's nanocenter proposal in 2000, he was considered as a co-founder of the Center for Functional Nanomaterials (CFN) at BNL. He acted as the Facility Leader and the group leader for the Electron Microscopy Facility at CFN. He is also an inaugural fellow of Microscopy Society of America and a fellow of the American Physical Society. His research focuses on studies of nanoscale phenomena that control materials' functionality by applying advanced electron microscopy and related techniques.